# DYNAMIC MATERIAL POINT METHOD WITH APPLICATIONS IN GEOMECHANICS

I. Jassim
*Deltares, Delft, The Netherlands / Institute of Geotechnics, Stuttgart University, Germany*

F. Hamad
*Deltares, Delft, The Netherlands / Institute of Geotechnics, Stuttgart University, Germany*

P. Vermeer
*Deltares, Delft, The Netherlands / Institute of Geotechnics, Stuttgart University, Germany*

**ABSTRACT:** *A dynamic Material Point Method for use in Geomechanics is presented. Soil and structural bodies are represented by (material) particles, which move inside an unstructured mesh of four-noded 3-D tetrahedral elements. As such low-order elements tend to show locking for fully developed plastic flow, a strain-enhancement remedy is described. As a first example, the penetration of a drop anchor into a Mohr-Coulomb soil is considered. As both a soil body and a metal anchor are considered, an algorithm for dynamic contact is used and described. An improved type of absorbing boundaries to avoid the reflection of stress waves is also described. The second example consists of dynamic cone penetration. Finally, the example of a collapsing tunnel is considered.*

## 1   INTRODUCTION

Over the last decades the Finite Element Method (FEM) has become the standard tool of analysis in the field of solid mechanics. However, due to its reliance on a mesh, the FEM is not well suited for the treatment of extremely large deformations. To overcome the mesh dependency of the FEM, meshfree methods have been developed, for example the Element-Free Galerkin Method (Belytschko et al, 1994) and the Material Point Method (MPM). The latter might be classified as a meshfree method, a Particle-in-Cell method or an Arbitrary Lagrangian-Eulerian method (Więckowski, 2004).

   MPM uses two discretizations of the material, one based on a computational mesh and the other based on a collection of material points or "particles". Within the standard MPM large deformations are modeled by particles moving through a fixed mesh. The particles carry all the properties of the continuum (material properties and state of stress and strain) as well as external loads, whereas the mesh and its Gaussian integration points carry no permanent information at all. The computational grid is used to determine incremental displacements of particles by solving the governing equations. Through this approach, MPM combines the advantages of both Eulerian and Lagrangian formulations.

   The early beginnings of MPM can be traced back to the work of Harlow (1964), who studied fluid flow by material points moving through a fixed grid. Sulsky et al. (1995) extended the method to the modeling of solids. It was then called the Material Point Method (Sulsky & Schreyer, 1996). Bardenhagen et al. (2000) further extended the method by including frictional contact between deformable bodies. The potential of MPM for simulating granular flow, e.g. in silo discharge, was first recognized by Więckowski et al. (1999). Coetzee et al. (2005) used the MPM for studying the large deformation problem of anchor

pull-out. All previous developments of MPM are based on dynamics, Beuth et al. (2010) were the first to develop a quasi-static MPM.

In Section 2 of this paper, the weak formulation and space integration of the momentum equation is presented. Section 3 describes integration in time. Here, explicit forward marching is used. A numerical example of a drop anchor is provided in Section 4. The formulation of a contact algorithm used to model the interaction between different bodies is explained in Section 5. In Section 6, mesh locking and strain smoothening are discussed. Absorbing boundaries and wave reflection are discussed in Section 7. A second numerical example is given in Section 8. In this example, dynamic cone penetration is investigated. Section 9 contains the example of a collapsing tunnel.

## 2    WEAK FORMULATION AND SPACE INTEGRATION OF EQUILIBRIUM

The Cauchy form of conservation of linear momentum is given by the equations

$$\rho\,\ddot{\mathbf{u}} = \nabla\cdot\boldsymbol{\sigma} + \rho\,\mathbf{g} \quad \text{and} \quad \mathbf{t} = \boldsymbol{\sigma}\cdot\mathbf{n} \tag{1}$$

where $\rho$ is the material density, $\mathbf{u}$ is the displacement, a superposed dot denotes differentiation with time, $\boldsymbol{\sigma}$ denotes the Cauchy stress tensor and $\mathbf{g}$ is the gravitational acceleration vector. The surface traction acting on the external boundary is denoted by $\mathbf{t}$ and $\mathbf{n}$ is the outward unit normal of the boundary. Applying the virtual work principle on a domain of volume $V$ surrounded by boundary $S$ yields

$$\int_V \delta\mathbf{u}^T \rho\,\ddot{\mathbf{u}}\,dV = -\int_V \delta\boldsymbol{\varepsilon}^T \boldsymbol{\sigma}\,dV + \int_V \delta\mathbf{u}^T \rho\,\mathbf{g}\,dV + \int_S \delta\mathbf{u}^T \mathbf{t}\,dS \tag{2}$$

where $\delta$ implies a virtual quantity, $\boldsymbol{\varepsilon}$ is the strain tensor and the script $T$ denotes the transpose.

For space discretisation, the displacement field $\mathbf{u}$ is approximated in terms of interpolation functions $\mathbf{N}$ and nodal displacements $\mathbf{a}$ by $\mathbf{u} = \mathbf{N}\mathbf{a}$. The strain tensor is now written in vector notation as

$$\boldsymbol{\varepsilon} = \mathbf{B}\,\mathbf{a} \quad \text{with} \quad \mathbf{B} = \mathbf{L}\mathbf{N} \quad \text{and} \quad \boldsymbol{\varepsilon} = \left(\varepsilon_{11},\ \varepsilon_{22},\ \varepsilon_{33},\ \gamma_{12},\ \gamma_{23},\ \gamma_{31}\right)^T \tag{3}$$

where $\mathbf{B}$ is the usual finite element strain-displacement matrix, as computed from the linear differential operator $\mathbf{L}$ and the shape functions $\mathbf{N}$. Substituting Eq. (3) into Eq. (2) gives

$$\delta\mathbf{a}^T \mathbf{M}\,\ddot{\mathbf{a}} = \delta\mathbf{a}^T\left(\mathbf{F}^{\text{ext}} - \mathbf{F}^{\text{int}}\right) \quad \text{or} \quad \mathbf{M}\,\ddot{\mathbf{a}} = \mathbf{F} \quad \text{with} \quad \mathbf{F} = \mathbf{F}^{\text{ext}} - \mathbf{F}^{\text{int}} \tag{4}$$

in which

$$\mathbf{M} = \int_V \rho\,\mathbf{N}^T \mathbf{N}\,dV, \quad \mathbf{F}^{\text{ext}} = \int_V \rho\,\mathbf{N}^T \mathbf{g}\,dV + \int_S \mathbf{N}^T \mathbf{t}\,dS \quad \text{and} \quad \mathbf{F}^{\text{int}} = \int_V \mathbf{B}^T \boldsymbol{\sigma}\,dV \tag{5}$$

Equation (4) is identically used within FEM and MPM. However, in the Material Point Method $\mathbf{M}$ can also change in size when particles move into empty elements. In other words, the total number of degrees-of-freedom of the system can vary. A lumped-mass matrix, which offers computational and storage advantages, is used instead of the consistent-mass matrix defined in Eq. (5). On denoting the entries of the lumped-mass matrix, as $m_i$ it yields

$$\mathbf{M}_L = \begin{bmatrix} m_1 & 0 & ... & 0 \\ 0 & m_2 & ... & 0 \\ \vdots & \vdots & & \vdots \\ 0 & 0 & ... & m_n \end{bmatrix} \tag{6}$$

where $n$ denotes the number of degrees of freedom. In order to conserve the mass of the continuum, particle-based integration is used i.e.

$$m_i \approx \sum_{p=1}^{n_p} m_p N_i^p \qquad \text{and} \qquad \mathbf{F}^{\text{int}} = \int_V \mathbf{B}^T \boldsymbol{\sigma} \, dV \approx \sum_{p=1}^{n_p} \mathbf{B}_p^T \boldsymbol{\sigma}_p V_p \tag{7}$$

where $n_p$ denotes the number of particles, $m_p$ is the mass of particle $p$, $N_i^p$ is the shape function evaluated at particle $p$ and $V_p$ is the volume associated with particle $p$. The drawback of using a lumped-mass matrix is a slight numerical dissipation of the kinetic energy (Burgess et al, 1992).

## 3 TIME INTEGRATION

On applying Euler-forward time integration with lumped-mass matrix, Eq. (4) yields

$$\dot{\mathbf{a}}^{t+\Delta t} = \dot{\mathbf{a}}^t + \Delta t \, \ddot{\mathbf{a}}^t, \qquad \ddot{\mathbf{a}}^t = \left[ \mathbf{M}_L^t \right]^{-1} \mathbf{F}^t \tag{8}$$

where $\Delta t$ is the current time increment, $\dot{\mathbf{a}}^t$ and $\dot{\mathbf{a}}^{t+\Delta t}$ are the nodal velocities at time $t$, $t+\Delta t$ respectively. The incremental nodal displacement is obtained by integrating the nodal velocity by the Euler-backward rule and the position of the particles are subsequently updated, i.e.

$$\Delta \mathbf{a}^{t+\Delta t} = \Delta t \, \dot{\mathbf{a}}^{t+\Delta t}, \qquad \mathbf{x}_p^{t+\Delta t} = \mathbf{x}_p^t + \mathbf{N}_p \, \Delta \mathbf{a}^{t+\Delta t} \tag{9}$$

where $\mathbf{x}_p^t$ and $\mathbf{x}_p^{t+\Delta t}$ are the particle positions at time $t$ and $t+\Delta t$ respectively. Strains and stresses at particles are updated using the same algorithms as for Gaussian integration points within the standard FEM. In updated Lagrangian FEM, one would use $\Delta \mathbf{a}$ to update the finite element mesh, but within the MPM only particles positions are updated. Particles eventually cross element boundaries, which entails that the new element of a crossing particle has to be detected.
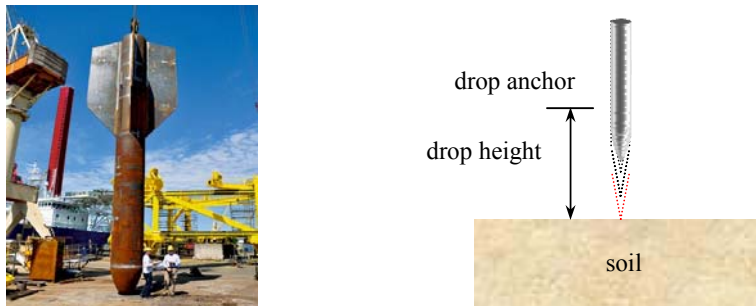


Fig. 1. A torpedo-shaped drop anchor

## 4    ANALYSIS OF DROP ANCHOR

The analysis of a drop anchor as shown in Figure 1 is presented in this section. These torpedo-shaped anchors are used in the offshore oil and gas industry as a cost effective anchoring solution in clays. The anchor is dropped from a particular height and penetrates the seafloor by the kinetic energy gained during its free fall (Figure 1). In the present paper, a fully dynamic penetration process is simulated. As the problem is axisymmetric, only a sector of $20^o$ is discretised. The drop anchor resembles a foundation pile, where soil deformations are intense around the tip. Accurate computations require a relatively dense mesh around the tip, as also shown in Figure 2a. Within the standard MPM, however, the anchor (particles) would move through the mesh and one would need mesh refinement over the complete penetration depth. In order to avoid this, we deviated from the standard MPM by using a mesh which is fixed to the anchor so that it moves into the soil. Thereby, the fine part of the mesh will always remain around the tip of the anchor. The occurrence of elements containing particles of different material is also prevented as the boundary of the anchor coincides throughout the analysis with element boundaries.

The material properties of the anchor are: Young's modulus of 50000 kPa, Poisson's ratio of 0 and unit weight of 78 kN/m³. The anchor is modeled as linear elastic. The soil is modeled by the Mohr-Coulomb model with a Young's modulus of 5000 kPa, Poisson's ratio of 0.3, cohesion of 5 kPa, friction angle of $30^o$ and unit weight of 18 kN/m³. Simulations were done with different friction coefficients $\mu$ of the contact surface between the anchor and the soil. Hence, we do not consider penetration in undrained clay, but in a drained sand. This is simply done because frictional sand is computationally more challenging than (undrained) cohesive clay.

Figure 3 shows the computed penetration depth for different $\mu$-values plotted over time. For fully rough contact ($\mu$=1), the final penetration depth is found to be 5D, where D is the diameter of the anchor. In the very beginning the anchor resistance is linear with penetration depth, but later the penetration is slowing down because the anchor looses its kinetic energy. As the anchor is penetrating deeper into the soil, the resistance is getting higher because the contact between anchor and soil is increasing and because the shear resistance of the soil increased with depth. The ultimate penetration depth obviously increases with smaller friction coefficients. The largest penetration depth obviously corresponds to the case of smooth contact. Figure 2b shows the particle distribution after a penetration of 6.5D for the case of smooth contact. It also shows soil heave around the anchor.
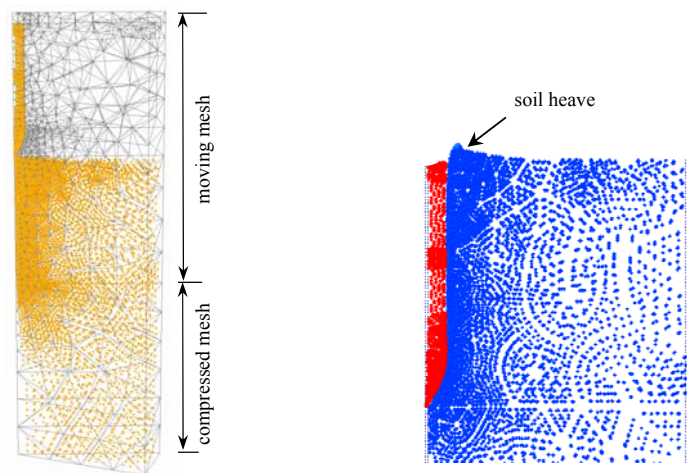


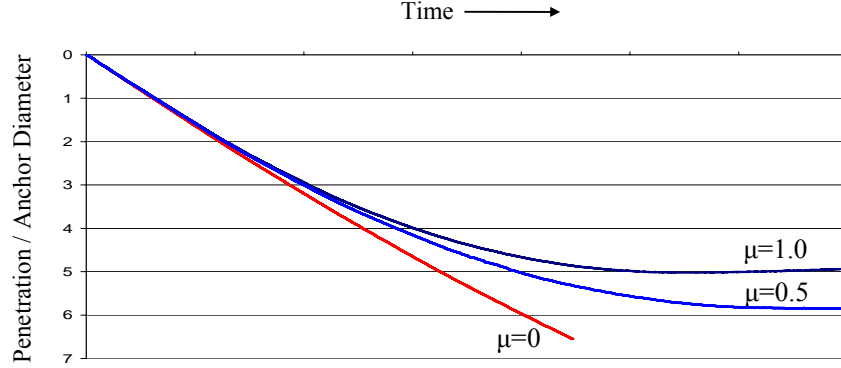Fig. 2.  Initial and final configuration of the problem

Fig. 3. Penetration depth for different values of the friction coefficient

## 5  CONTACT ALGORITHM

Following Bardenhagen et al. (2000), Eq. (8) is solved for the combined bodies *A* and *B* (see Figure 4) as well as for each body separately, i.e.

$$\mathbf{M}_L^A \, \ddot{\mathbf{a}}^A = \mathbf{F}^A, \qquad \mathbf{M}_L^B \, \ddot{\mathbf{a}}^B = \mathbf{F}^B, \qquad \mathbf{M}_L^{A+B} \, \ddot{\mathbf{a}}^{A+B} = \mathbf{F}^{A+B} \tag{10}$$

From these solutions, predictor velocities $\dot{\mathbf{a}}^A$, $\dot{\mathbf{a}}^B$ and $\dot{\mathbf{a}}^{A+B}$ are computed. Contact at a considered node is detected by comparing the velocity of a single body to the velocity of the combined bodies, as illustrated in the chart of Figure 5, with $\mathbf{n}$ being the outward unit normal at a considered node. When these velocities differ, the considered node is a contact node. Now we detect whether or not the contact at that node is broken (by separation) or continued (by approaching). For an approaching contact node, we check for sliding as explained in the next section.

### 5.1  Check for Sliding and Subsequent Correction for a Contact Node

In the following, only body *A* is considered. The relative normal and tangential velocities at a contact node are

$$\dot{\mathbf{a}}_n = \left[ \left( \dot{\mathbf{a}}^A - \dot{\mathbf{a}}^{A+B} \right) \cdot \mathbf{n} \right] \mathbf{n} \quad \text{and} \quad \dot{\mathbf{a}}_t = \left( \dot{\mathbf{a}}^A - \dot{\mathbf{a}}^{A+B} \right) - \dot{\mathbf{a}}_n \tag{11}$$

The normal and tangential components of the interaction force at a contact node can then be computed from

$$\mathbf{F}_n^A = \frac{m^A}{\Delta t} \, \dot{\mathbf{a}}_n \quad \text{and} \quad \mathbf{F}_t^A = \frac{m^A}{\Delta t} \, \dot{\mathbf{a}}_t \tag{12}$$

where $m^A$ is the mass of a contact node computed only from body *A* as in Eq. (7). In frictional contact, the tangential force is limited by

$$\left| \mathbf{F}_t^{A,max} \right| = \mu \left| \mathbf{F}_n^A \right| = \mu \frac{m^A}{\Delta t} \left[ \left( \dot{\mathbf{a}}^A - \dot{\mathbf{a}}^{A+B} \right) \cdot \mathbf{n} \right] \tag{13}$$

where $\mu$ is the coefficient of friction. Sliding between the two bodies will only occur when $\left|\mathbf{F}_t^A\right| > \left|\mathbf{F}_t^{A,\max}\right|$. Thus, only then a correction of the nodal velocity is required. It can be derived that the corrected velocity of a sliding contact node is

$$\dot{\mathbf{a}}_{new}^A = \dot{\mathbf{a}}^A - \left[\left(\dot{\mathbf{a}}^A - \dot{\mathbf{a}}^{A+B}\right)\cdot\mathbf{n}\right](\mathbf{n} + \mu\,\mathbf{t}) \qquad (14)$$

where $\mathbf{t}$ is the direction vector of the tangential velocity.
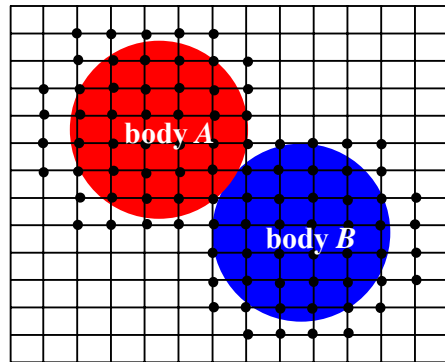


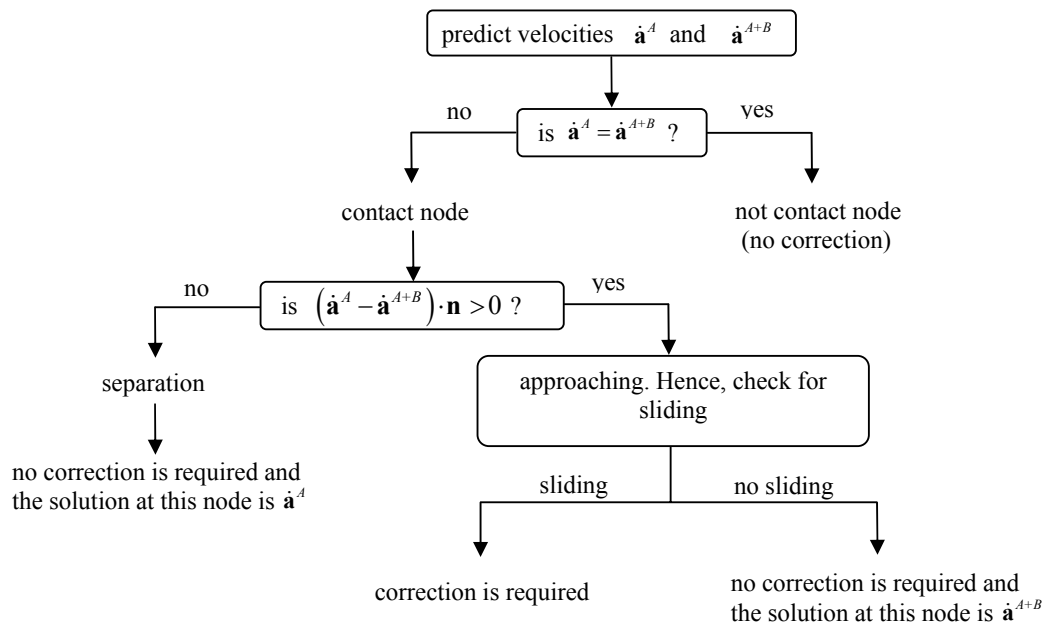Fig. 4. Illustration of two bodies in contact for a regular mesh



Fig. 5. Flow chart of the contact algorithm applied on body $A$

## 6 MESH LOCKING AND STRAIN SMOOTHENING

Difficulties arise when determining the displacement field for a solid that is nearly incompressible. For such a material, the bulk modulus is very large and small errors in strain will yield large errors in stress. Furthermore, when dealing with low-order elements the mesh may lock when incompressibility constraints from neighboring elements are imposed. For high-order elements, it is common to prevent locking by reduced integration (Bathe, 1982), but for low-order elements a kind of strain smoothening can be applied, being referred to as nodal-mixed-discretisation by Detournay and Dzik (2006). This technique involves first of all the computation of the strain rates for each element in the usual manner subsequently they are decomposed into a volumetric strain rate, $\dot{\varepsilon}_v$, and a deviatoric strain rate, $\dot{\mathbf{\varepsilon}}_d$. An averaged volumetric strain-rate $\bar{\dot{\varepsilon}}_v$ for an element is now defined as

$$\bar{\dot{\varepsilon}}_v = \frac{1}{4}\sum_{i=1}^{4}\bar{\dot{\varepsilon}}_{vi} \quad \text{with} \quad \bar{\dot{\varepsilon}}_{vn} = \frac{\sum_k (\dot{\varepsilon}_v \Omega)_k}{\sum_k (\Omega)_k} \tag{15}$$

where the sum is over all elements $k$ attached to the node $n$. $\Omega$ is the volume of an element. The working assumption is that deviatoric strain rates need not be enhanced, only the volumetric components. As a result, the final strain rate within an element is redefined as

$$\dot{\mathbf{\varepsilon}} = \dot{\mathbf{\varepsilon}}_d + \frac{1}{3}\bar{\dot{\varepsilon}}_v \mathbf{I} \quad \text{with} \quad \mathbf{I} = (1, 1, 1, 0, 0, 0)^T \tag{16}$$

This approach is applied in all examples of the present paper.

## 7 ABSORBING BOUNDARIES

In numerical simulations of wave propagation, the use of finite boundaries leads to reflection of the waves upon reaching the boundary. In Geomechanics rigid boundaries are mostly numerical antifacts and reflecting waves are not physical and they will affect the solution considerably. This problem might be overcome by choosing the finite boundary of the mesh far enough so that no reflection occurs. But this is not always practical solution as it makes the mesh unnecessarily large. On top of that, the computational effort increases considerably. A partial solution to this problem was introduced by Lysmer and Kuhlemeyer (1969). They proposed a solution in which the boundary is supported on a dashpot. On denoting the normal stress at a boundary node as $t_n$ and the shear stress as $t_s$, it yields

$$t_n = \alpha_n \rho V_p \dot{a}_n \quad \text{and} \quad t_s = \alpha_s \rho V_s \dot{a}_s \tag{17}$$

where $\dot{a}_n$ and $\dot{a}_s$ are the normal and tangential velocities at a boundary node respectively, $\rho$ is the mass density of the material, $\alpha_n$ and $\alpha_s$ are dimensionless parameters, $V_p$ and $V_s$ are the p-wave speed and the s-wave speed of the material respectively. It yields

$$V_p = \sqrt{E_c/\rho} \quad \text{and} \quad V_s = \sqrt{G/\rho} \tag{18}$$

where $E_c$ is the constrained modulus and $G$ is the shear modulus. They relate to Young's modulus and Poisson's ratio by the equations

$$E_c = \frac{(1-\upsilon)E}{(1-2\upsilon)(1+\upsilon)} \quad \text{and} \quad G = \frac{E}{2(1+\upsilon)} \tag{19}$$

The drawback of supporting the boundary by dashpots is that the boundary will continuously creep as long as the dashpot will receive stresses from the soil body. In order to limit the creep of the boundary, a spring is added parallel to the dashpot to obtain a Kelvin-Voigt type of boundary response. Hence Eq. (17) is rewritten as

$$t_n = \alpha_n \rho V_p \dot{a}_n + \frac{E_c}{\delta_n} a_n \quad \text{and} \quad t_s = \alpha_s \rho V_s \dot{a}_s + \frac{G}{\delta_s} a_s \tag{20}$$

where $\delta$ is a virtual thickness being used to limit the creep of the boundary.

As a numerical example a soil layer with a thickness of 1m is considered here. The layer has a Young's modulus of 100 kPa, a Poisson's ratio of 0 and unit weight of 18 kN/m³. A uniformly distributed load of 1 kPa is applied instantaneously at the surface. Three different boundary conditions were considered at the bottom: fully fixed, dashpot and dashpot with spring in parallel. With the fully fixed boundary, the entire energy is reflected when the wave reached the bottom. Hence, the stress is doubled after reflection and oscillates later contineously. When replacing the fixities by dashpots, only a small portion of the energy is reflected, but (as explained previously), the drawback of using only dashpots is a continuous creep of the boundary.

On the other hand, the dashpot with spring in parallel will limit the creep of the boundary as shown in Figure 6. This displacement corresponds to $\delta_n = 0.5$ m and $\alpha_n = 2.5$. Sensitivity study showed that those are the best values for the problem considered. The final displacement of the bottom of the mesh can be calculated as $a_n = (\sigma / E_c)\, \delta_n$. For $\sigma = 1$kPa and $E_c = 100$kPa, this displacement is found to be 0.05 m. Points 1,2 and 3 of Figure 6 indicate that the wave is just reflected after reaching the bottom of the mesh. Stress fronts correspond to point 1, 2 and 3 are (1.28, 1.86 and 1.14) kPa respectively.
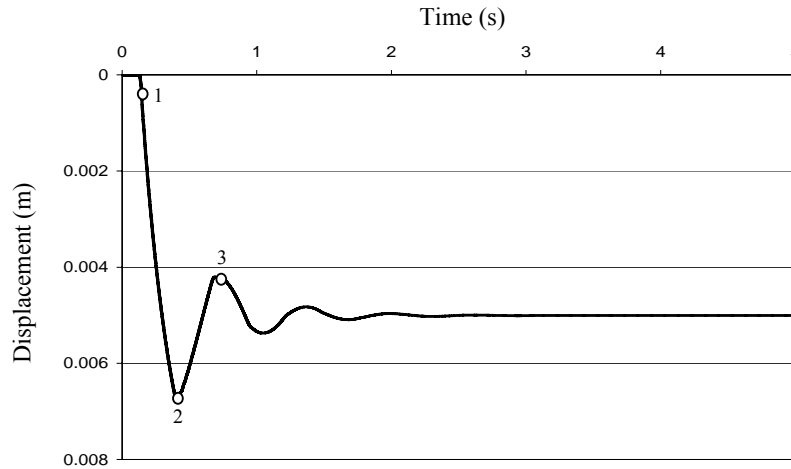


Fig. 6. Displacement of the bottom of the mesh for dashpot and spring in parallel

## 8    DYNAMIC PENETRATION TEST

The analysis of a cone (with a diameter of 3.57 cm) being hammered into the soil is considered in this section. Block is successively dropped from a certain height as shown in Figure 7. The maximum impulsive load, $F_{max}$, corresponding to the drop weight, can be calculated from the conservation of momentum i.e.

$$\int_{0}^{t_{pulse}} F_{\max} \, \sin\left(\frac{\pi t}{t_{pulse}}\right) dt \;=\; \eta \, m \sqrt{2gh} \tag{21}$$

where $\eta$ is the hammer efficiency (fraction of energy transferred to the cone). It was chosen as 64% (Borja, 1988). The initial configuration of the problem is shown in Figure 8a. The same moving mesh technique used to simulate the drop anchor problem of Section 4 is used here. The material properties of the elastic cone are: Young's modulus of 50000 kPa, Poisson's ratio of 0 and unit weight of 78 kN/m³. Adopting the elastic-plastic Mohr-Coulomb model, the soil properties are: Young's modulus of 5000 kPa, Poisson's ratio of 0.3, cohesion of 5 kPa, friction angle of $30^{o}$ and unit weight of 18 kN/m³. The dropped weight has a mass $m$ =10 kg, the drop height $h$ = 50 cm, $t_{pulse}$ = 0.02 sec and $t_{period}$ = 0.1 sec. The case of fully rough contact, $\mu$=1, between the cone and the soil is considered. Figure 9 shows the penetration verses the number of blows. Figure 8b shows the principal stresses at the end of the penetration.
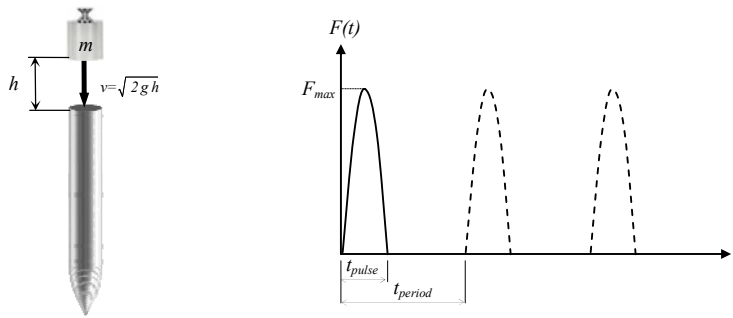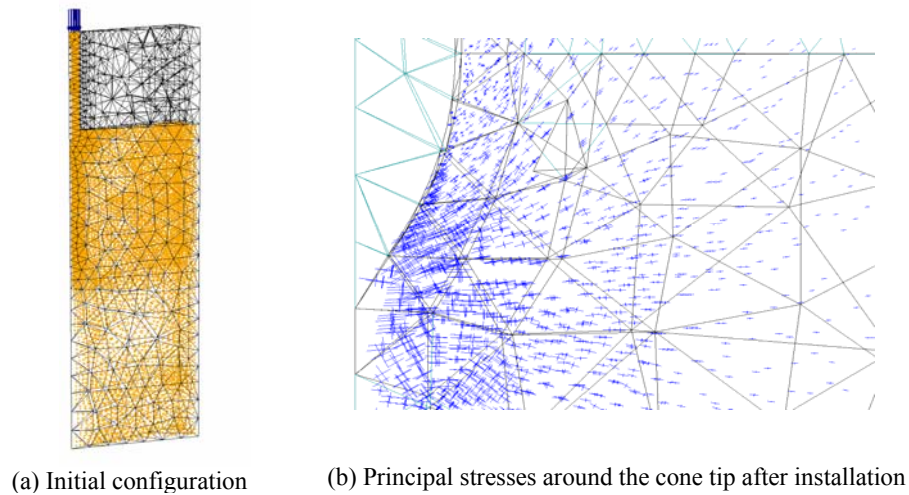


Fig. 7. Applied load of dynamic penetration test



(a) Initial configuration        (b) Principal stresses around the cone tip after installation

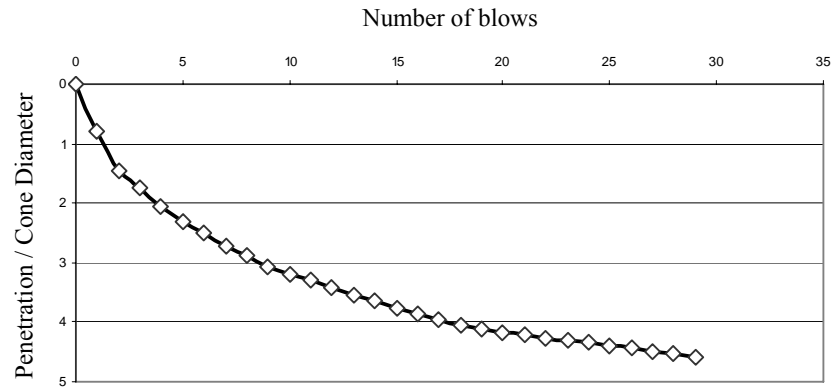Fig. 8. Initial configuration and final state of stress

Fig. 9. Penetration as a function of number of blows

## 9    DYNAMIC COLLAPSE OF TUNNEL FACE

Tunnel collapse can pose a danger to life and property. Both the life of the workers standing in front of the tunnel face and individuals at the ground surface might be in danger. An example of tunnel collapse in Munich is shown in Figure 10. The aim of this analysis is to estimate the real collapse time of a tunnel and the crashing of the ground. The pattern of the tunnel face collapse is also investigated. The dimensions of the tunnel mesh are shown in Figure 11. The boundary conditions are: the upper surface is free to move, the side surfaces are roller supported, and the base is fixed.

In the first stage of the analysis, initial stresses are generated based for a $K_o$-value of 0.5, where $K_o$ is the co-efficient of lateral earth pressure at rest. Adopting the elastic-plastic Mohr-Coulomb model, the soil properties are: Young's modulus of 10000 kPa, Poisson's ratio of 0.3, cohesion of 1 kPa, friction angle of $25^o$ and unit weight of 16 kN/m$^3$. A relatively fine mesh is used to discretise the material around the opening of the tunnel where the material is expected to flow. The face support pressure is removed in single step and the calculation is carried out by applying time steps of $\Delta t$=0.001 second. For time increment, the particles move due to the unbalanced forces in the system until the kinetic energy is dissipated and static equilibrium is reached. The total displacements for the final static equilibrium are shown in Figure 12a. The collapse time for the tunnel face is found to be 7 seconds. The settlement of the ground surface is shown in Figure 12b.



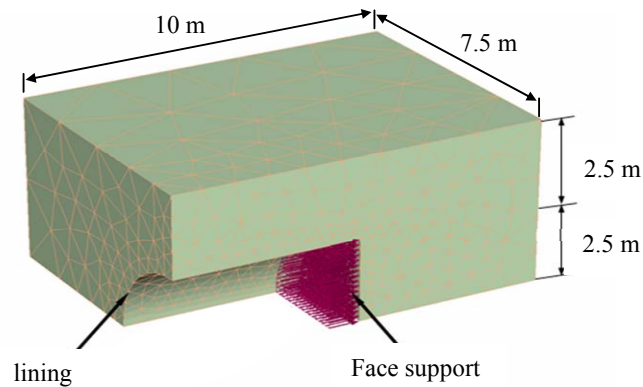Fig. 10. Collapse of tunnel face Munich underground in September 1994
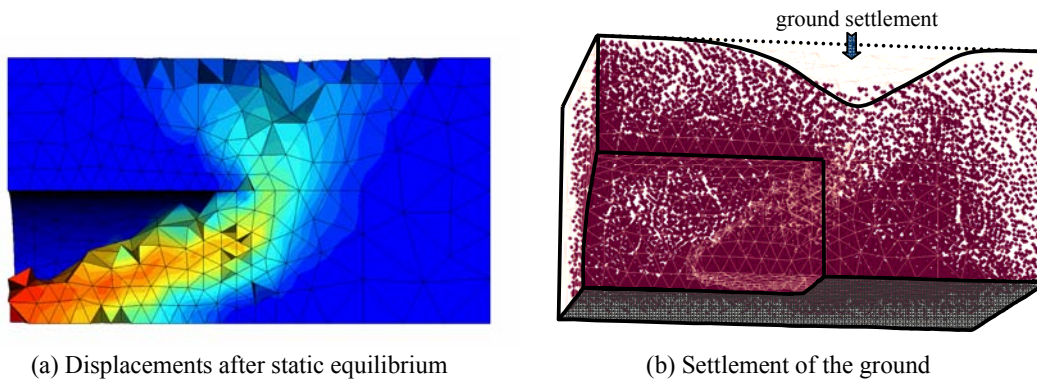
Fig. 11. Description of tunnel geometry



(a) Displacements after static equilibrium                    (b) Settlement of the ground

Fig. 12. Pattern of the tunnel face collapse

## 10  CONCLUSIONS

Existing dynamic MPM codes are based on a regular grid. For complex structures, being represented by a cloud of material particles, this would require a special CAD type preprocessor. On the other hand existing user-friendly preprocessors can be used in combination with non-regular and non-structured meshes. This is the main reason for the use of the non-structured meshes. Another advantage of the present non-structured mesh approach is that it allows for mesh-refinements. In this paper this has been applied for reason of achieving good accuracy in zones of intense soil deformations. For a consequent application of mesh refinement, the concept of moving mesh has been introduced.

In dynamic soil analyses one usually introduces absorbing boundaries to prevent the reflection of stress and strain waves at the more or less arbitrary bottom of the mesh. Hence, one usually employs so-called dashpots that will continually creep under load. In order to limit such non-physical displacements, the dashpot is combined with a spring to obtain a Kelvin-Voigt type of boundary response. At present the main limitations of the code is the lack of pore pressures and a soil model for cyclic loading. Meanwhile, dynamic generation and dissipation of pore pressures is nearly finished and remains to be reported. The implementation of a cyclic loading model for genuine simulations of pile driving has been planned.

## ACKNOWLEDGEMENT

## REFERENCES

Bardenhagen, S.G. Brackbill, J.U. & Sulsky, D. (2000), "The material-point method for granular materials''. Computer Methods in Applied Mechanics and Engineering, Vol.(187), 529–541.

Bathe, K.J. (1982), Finite Elements Procedures in Engineering Analysis, Prentice-Hall, Inc., New Jersey.

Belytschko, T. Lu, Y. Y. & Gu, L. (1994), "Element-free Galerkin methods''. International Journal of Numerical Methods in Engineering, Vol. (37), 229-256.

Beuth, L., Więckowski, Z. & Vermeer, P. (2010), "Solution of quasi-static large-strain problems with the material point method''. International Journal of Numerical and Analytical Methods in Geomechanics, Wiley Online Library (wileyonlinelibrary.com). DOI: 10.1002/nag.965

Borja, R.I. (1988), "Dynamics of pile driving by the finite element method''. Computers and Geotechnics, Vol. (5), 39-49.

Burgess, D. Sulsky, D. & Brackbill, J.U. (1992), "Mass matrix formulation of the FLIP particle-in-cell method''. Journal of Computational Physics, Vol. (103), 1-15.

Coetzee, C.J. Vermeer, P.A. & Basson, A.H. (2005), "The modelling of anchors using the material point method''. International Journal for Numerical and Analytical Methods in Geomechanics, Vol. (29), 879-895.

Detournay, C. & Dzik E. (2006), "Nodal mixed discretization for tetrahedral elements'', Proceedinh of '4 international FLAC symposium on numerical modeling in geomechanics, Itasca Consulting Group.

Harlow, F.H. (1964), "The particle-in-cell computing method for fluid dynamics''. Methods for Computational Physics, Vol. (3), 319-343.

Lysmer, J. & Kuhlmeyer, R.L. (1969), "Finite dynamic model for infinite media''. Journal of the Engineering Mechanics Division, Vol. (95), 859-877.

Sulsky, D. Zhou, S.J. & Schreyer, H.L. (1995), "Application of a particle-in-cell method to solid mechanics''. Computer Physics Communications, Vol. (87), 236-252.

Sulsky, D. & Schreyer, H.L. (1996), "Axisymmetric form of the material point method with applications to upsetting and Taylor impact problems''. Computer Methods in Applied Mechanics and Engineering, Vol. (139), 409-429.

Więckowski, Z. Youn, S.K. & Yeon, J.H. (1999), "A particle-in-cell solution to the silo discharging problem''. International Journal for Numerical Methods in Engineering, Vol. (45), 1203-1225.

Więckowski, Z. (2004), "The material point method in large strain engineering problems''. Computer Methods in Applied Mechanics and Engineering, Vol. (193), 4417-4438.